Eur. Phys. J. B **10**, 397–408 (1999)

THE EUROPEAN PHYSICAL JOURNAL B

EDP Sciences

Charge ordering-disordering in the Th-doped $CaMnO_3$

M. Hervieu[1,a], C. Martin[1], A. Maignan[1], G. Van Tendeloo[2], and B. Raveau[1]

[1] Laboratoire CRISMAT[b], ISMRA et Université de Caen, 6 boulevard du Maréchal Juin, 14050 Caen Cedex, France
[2] EMAT, University of Antwerp (RUCA), Groenenborgerlaan 171, 2020 Antwerp, Belgium

Received 2 November 1998

Abstract. The structural transitions that appear in the manganites $Ca_{1-x}Th_xMnO_3$ *versus* temperature are studied in connection with their magnetic and transport properties, and compared to those of the $Ca_{1-x}Ln_xMnO_3$ manganites. An orthorhombic to monoclinic transition is observed for low x values ($x \approx 0.08$); this structural distortion, also observed for Ln-doped oxides, is related to the magnetoresistance properties. For higher x values ($0.15 \leq x \leq 0.30$), modulated commensurate and incommensurate phases are obtained at low temperature, with $a = 1/qa_p\sqrt{2}$, $b = 2a_p$ and $c = a_p\sqrt{2}$, which are related to Mn^{3+}/Mn^{4+} charge ordering (CO) phenomena. T_{CO} values, determined from electron diffraction, are in agreement with those determined from the $M(T)$ curves. The low temperature electron microscopy shows that the CO in those oxides is more complex than in Ln-doped manganites. In particular, the destabilisation of CO and consequently of the antiferromagnetic interactions is evidenced as the thorium content increases which may explain the appearance of a spin-glass like behavior for higher x values ($x \approx 0.25 - 0.30$) not seen for $Ca_{1-x}Sm_xMnO_3$ phases ($x \approx 0.50 - 0.60$).

PACS. 61.14.-x Electron diffraction and scattering – 75.30.-m Intrinsic properties of magnetically ordered materials – 72.20.My Galvanomagnetic and other magnetotransport effects

1 Introduction

Recently, the manganites of perovskite structure, $Ln_{1-y}A_yMnO_3$ (Ln and A are trivalent lanthanides and divalent alkaline-earth ions, respectively), have been the purpose of numerous studies according to their colossal magnetoresistance (CMR) [1–5]. The substitution of A^{2+} for Ln^{3+} is responsible for the partial hole filling of the e_g conducting band and above a critical hole concentration an insulator to metal transition associated to a paramagnetic to ferromagnetic transition is achieved. The ferromagnetism of these hole-doped compounds is due to the double exchange Mn^{3+}-O-Mn^{4+} interaction [6] and they exhibit CMR in the vicinity of T_C.

However, for sufficiently small A-site average ionic radius ($\langle r_A \rangle$), the hole doping does not induce the ferromagnetic metallic state as previously shown, for $Ln_{0.7}A_{0.3}MnO_3$ phases [7]. In this respect, the study of the $Pr_{1-x}Ca_xMnO_3$ series of small $\langle r_A \rangle$ by Jirak *et al.* [8] revealed the existence of structural transitions due to charge ordering (CO), *i.e.* ordering of the Mn^{3+} and Mn^{4+} species below T_{CO}. For $x = 0.5$, the CO model involving a 90° ordering of the d_z^2 Mn^{3+} orbitals was initially proposed by Goodenough [9] in order to interpret the CE-type antiferromagnetism of $La_{0.5}Ca_{0.5}MnO_3$ [10]. Moreover, the recent observations by electron diffraction (ED) and lattice imaging at low temperatures, showing the existence of several kinds of long range charge ordering in the form of Mn^{3+}/Mn^{4+} stripes in Mn(IV) rich compounds $Ca_{1-x}Ln_xMnO_3$ with Ln = La and Sm [11,12], strongly suggest that the charge localisation phenomena are responsible for the insulating behaviour. The lack of CMR properties is related to the stability of these CO phases for $0.25 \leq x \leq 0.50$.

CMR properties were also evidenced more recently in the Mn(IV) rich perovskites $Ca_{1-x}Sm_xMnO_3$ [13] with $x < 0.25$, showing resistance ratio close to 10^2 at 50 K. In fact, this exploration was based on the results obtained for the Mn(IV)-rich $Ca_{1-x}Bi_xMnO_3$, whose magnetic and transport properties [14–17] are of great interest. More particularly, it was shown by Chiba *et al.* [17] that this bismuth doped $CaMnO_3$ exhibits ferromagnetism and magnetoresistance, with $R_0/R_{7T} = 3$ at 50 K. The fact that a similar magnetoresistance ratio, $R_0/R_{12T} \approx 4$ at 30 K, exists for $Ca_{1-x}Eu_xMnO_3$ [18], has encouraged a more systematic exploration of the electron doped manganites.

Although they generally exhibit a smaller magnetoresistance ratio than the hole doped manganites, the study of electron doped ones is important for the understanding of the mechanisms which govern the CMR properties. The systematic exploration of the perovskites $Ca_{1-x}Ln_xMnO_3$ and $Ca_{1-x}Th_xMnO_3$ showed that electron concentration

[a] e-mail: `hervieu@crismat.ismra.fr`
[b] UMR 6508 associée au CNRS

is a predominant factor governing the CMR in these manganites of small $\langle r_A \rangle$ [19]. The electron concentration is directly related to the valence of the doping element so that only half the amount of Th(IV) – compared to Ln(III) – is necessary to reach the optimal CMR, *i.e.* $x \sim 0.15$ and $x \sim 0.08$ for $Ca_{1-x}Ln_xMnO_3$ and $Ca_{1-x}Th_xMnO_3$, respectively.

Thorium, owing to its tetravalent character, is susceptible to influence differently the charge ordering phenomena, compared to the trivalent lanthanides. In this paper, we are using electron microscopy to describe the charge ordering phenomena which appear in the manganites $Ca_{1-x}Th_xMnO_3$, in connection with the magnetotransport properties. We show that the oxides with $0.08 < x < 0.15$ exhibit short range ordering similar to that observed for $Ca_{1-x}Sm_xMnO_3$ ($0.20 \leq x < 0.25$) [12]. For higher Th content, $0.20 \leq x \leq 0.30$, one observes also long range ordering as in the $Ca_{1-x}Sm_xMnO_3$ modulated phases, involving Mn^{3+} and Mn^{4+} stripes along **a**, either in a commensurate or in an incommensurate way. Nevertheless the evolution of the modulation vector qa^* *versus* electron carrier density and *versus* T is different from that of $Ca_{1-x}Sm_xMnO_3$. Moreover at low temperature, $T = 40$ K, a spin glass behaviour is observed for $x \approx [0.25{-}0.30]$.

2 Experimental procedure

Polycrystalline samples $Ca_{1-x}Th_xMnO_3$ were synthesized from stoichiometric mixtures of ThO_2, CaO and MnO_2. The mixtures with nominal compositions $Ca_{1-x}Th_xMnO_3$ ($0.08 \leq x \leq 0.30$) were first heated at 1000 °C, sintered at 1200 °C, then at 1500 °C for 12 hours, slowly cooled down to 800 °C and then quenched to room temperature. Single phases are obtained for $0.0 \leq x < 0.30$. The $x = 0.30$ composition is considered as the limit of the homogeneity range since minority phases are observed (about 4% according to X-ray powder patterns).

One should note that the structural and microstructural characterizations as well as the physical properties measurements reported herein were carried out on the as-synthesized samples, without any further annealing which could modify the CO [20]. However iodometric titrations show that the oxygen content is O_3, in the limit of accuracy of the method.

Samples for electron microscopy study were prepared by smoothly crushing the crystallites in alcohol. The small flakes were deposited on a holey carbon film, supported by a copper grid. The electron diffraction (ED) study of the samples $Ca_{1-x}Th_xMnO_3$, $0.08 \leq x \leq 0.3$, was carried out at room temperature with a JEOL 200CX electron microscope, using a tilting-rotating sample holder (tilt ±60° and rotation ±180°). The ED study as a function of temperature and the bright/dark field imaging was made with a JEOL 2010 electron microscope fitted with a double tilt cooling sample holder (±40° for 92 K $\leq T \leq$ 300 K). The ED patterns were recorded *versus* T keeping a constant electron current density. The positions of the spots in electron diffraction patterns were measured from films

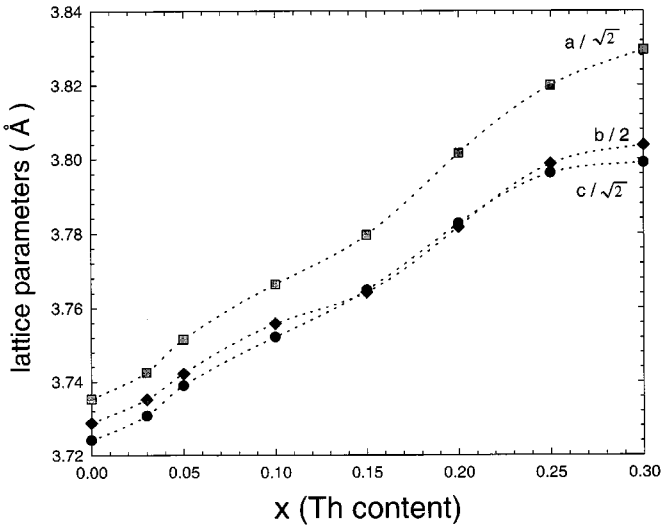

Fig. 1. $Ca_{1-x}Th_xMnO_3$: perovskite subcell parameters ($a/\sqrt{2}$, $b/2$ and $c/\sqrt{2}$ of the Pnma-type orthorhombic cell) *vs.* x.

by using video processor TAMPON Fotovix II X-S. This CDD image has a 470,000 pixels high resolution for a 6 times maximum enlarging. Each value corresponds to a minimum of 10 average measurements in the ED patterns, without any important standard deviation. All the scans were carried out following the same experimental conditions, *i.e.* increasing the temperature from 92 K to 300 K, waiting for the temperature stabilization before each ED recording, made with a constant electron beam adjustment. For the different samples, experiments with long exposure times were carried out to investigate a possible influence of the electron irradiation on the different phenomena observed. In the present samples, no significant effect was detected.

The high resolution electron microscopy (HREM) study was made with a TOPCON 002B electron microscope operating at 200 kV (Cs = 0.4 mm). Image calculations were carried out with the MacTempas software.

The three transmission electron microscopes are equipped with energy dispersive spectroscopy (EDS) analysers. For each of the samples, EDS analyses were systematically performed on about thirty grains.

The X-ray powder diffraction (XRPD) data were collected at room temperature with a Philips diffractometer (CuKα radiation) in the range $10° \leq 2\theta \leq 110°$ by increment of $0.02°(2\theta)$.

The resistivity measurements were performed from room temperature down to 5 K, by the four probe method on sintered bars, in the earth magnetic field or in 7 T. The magnetization *versus* temperature was registered on warming with a vibrating sample magnetometer in a magnetic field of 1.4 T or 10^{-2} T, which was applied at 4.2 K after a zero field cooling. Ac susceptibility-curves were registered with an AC/DC-SQUID magnetometer from Quantum Design.

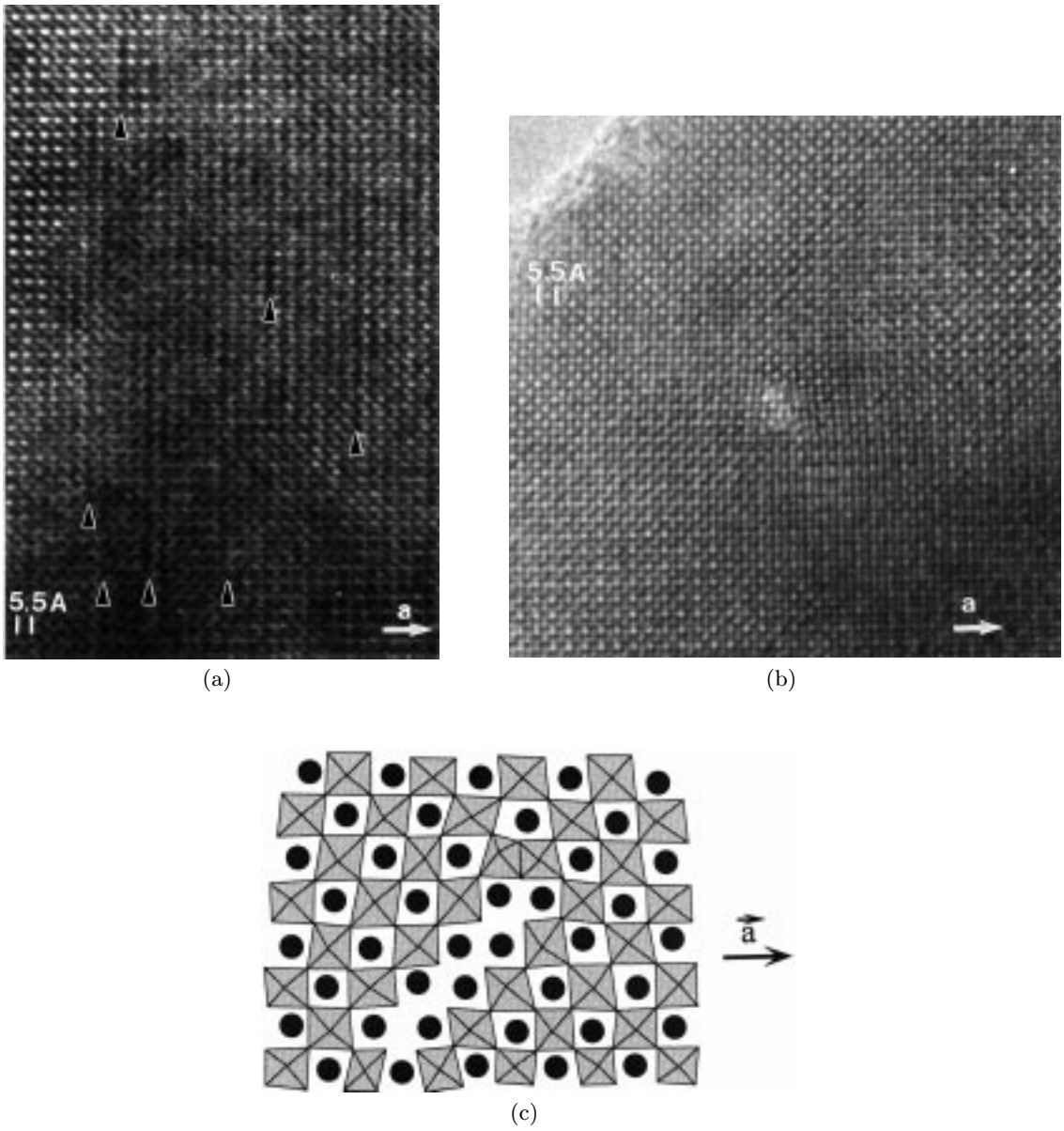

(a) (b) (c)

Fig. 2. [010] HREM of the $x = 0.15$ sample, recorded at room temperature: examples of defects (a) formation of short segments a few nanometers long along **c** associated with streaks in the ED patterns. (b) dislocation like defects and (c) model corresponding to the local formation of a rock salt additional layer.

3 Results and discussion

3.1 Preliminary structural characterization at room temperature

The systematic XRPD and ED investigations show that the samples $Ca_{1-x}Th_xMnO_3$ are monophasic for $0 \leq x < 0.30$. The EDS analyses confirm their homogeneity. The $x = 0.30$ composition, for which traces of a secondary phase are detected, can be considered as the limit of the homogeneity range.

Similar to the $Ca_{1-x}Ln_xMnO_3$ perovskites, the present compounds crystallize in the Pnma-type orthorhombic cell, with $a \sim a_p\sqrt{2}$, $b \approx 2a_p$ and $c \approx a_p\sqrt{2}$, where a_p is the parameter of the ideal cubic perovskite. The perovskite subcell parameters "$a/\sqrt{2} \times b/2 \times c/\sqrt{2}$" (Fig. 1) increase as x increases, due to the Mn^{3+} for Mn^{4+} substitution. The distortion of the cell, rather weak for low x values, increases slightly with x; the a and c parameters remain very close. This behavior is different from the one observed for $Ca_{1-x}Sm_xMnO_3$, where a rather strong orthorhombic distortion is observed as x increases [12].

The ED and HREM studies also confirm the good crystallinity of the samples which exhibit the classical contrast of the Pnma-type structures. They show the existence of twinning domains, with twin boundaries

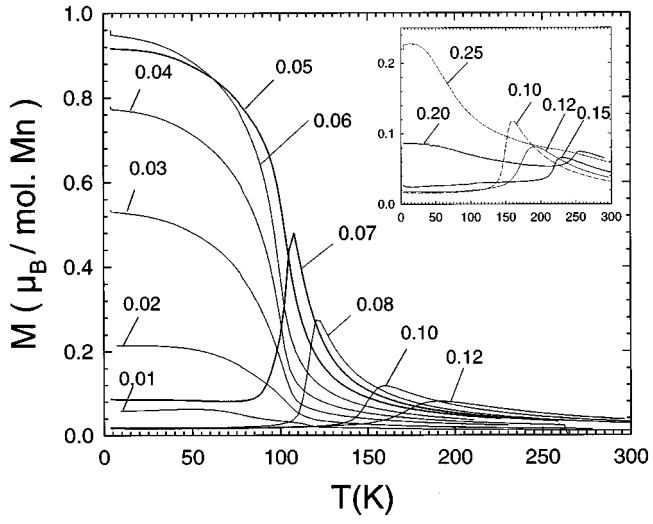

(a)

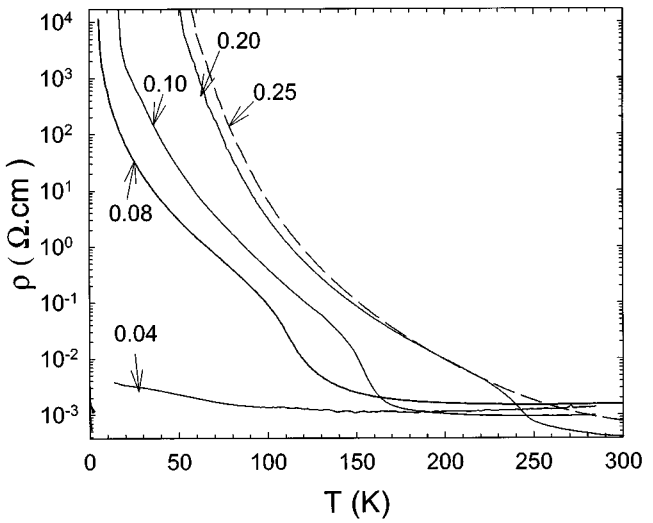

(b)

Fig. 3. $Ca_{1-x}Th_xMnO_3$: T dependence of (a) the magnetization under 1.45 T and (b) the resistivity. (x values are labelled on the graph).

parallel to the equivalent $(001)_p$, as usually observed in these orthorhombically distorted perovskites [21–23]. However, very weak diffuse streaks along [100]* are often observed in the [010] ED patterns. They are associated with a strained contrast in the corresponding bright field images. The enlargements of HREM images show that the contrast is only locally modified, in the form of short segments a few nanometers long along **c** (see arrows Fig. 2a). This phenomenon could be compared to the one systematically observed in the Pr and Nd-based manganites [21], which has been interpreted as a charge segregation. The defective rows are "$2a$" to "$5a$" spaced and often suffer translations along **a**, similar to those observed at low temperature (see further section and Ref. [20]). An accurate study of these phenomena is in progress.

Dislocation like defects are also observed, as shown in the [010] image of Figure 2b where the high electron density zones are imaged as bright dots. The interruption of atomic rows along [001] or [101] is easily visible by viewing the image under grazing incidence. These defects can simply be interpreted by the local formation of intergrowth rock salt-type defects within the perovskite matrix (Fig. 2c).

3.2 $Ca_{0.92}Th_{0.08}MnO_3$: Orthorhombic to monoclinic transition associated to a metal to insulator transition

The previous study by AC-χ susceptibility and resistivity of the oxides $Ca_{1-x}Sm_xMnO_3$ with $0 \leq x \leq 0.12$ has shown that doping e_g electrons in the insulating $CaMnO_3$ leads to a metallic behavior with non saturated ferromagnetism [24] which contrasts with the insulating behavior of their Mn(III) rich counterparts. This difference has been recently ascribed to orbitally degenerated e_g levels of slightly electron doped $CaMnO_3$ [25]. In this respect, the cluster-glass state observed for the electron concentrations ($0.07 \leq x \leq 0.12$) [24] may result from a canting of the C-type structure as predicted from reference [25]. A similar non saturated ferromagnetism is also observed in $Ca_{1-x}Th_xMnO_3$ ($0 < x < 0.07$) [19]. For higher electron concentrations corresponding to $x > 0.12$ in $Ca_{1-x}Sm_xMnO_3$ or to $x \geq 0.07$ in $Ca_{1-x}Th_xMnO_3$, an antiferromagnetic insulating state develops at the expense of the semimetallic ferromagnetic one, so that peak shaped $M(T)$ curves are observed (Fig. 3a). It must be pointed out that the best CMR properties of these Mn(IV) rich series are obtained for about the same electron concentration corresponding to $x = 0.15$ and $x = 0.08$ for Sm [13] and Th [19], respectively. These compositions are thus on the border between ferromagnetic and antiferromagnetic regions.

The present ED study *versus* temperature of the $Th_{0.08}$ CMR compound demonstrates that Th-doping leads to the same structural effect as Sm doping, *i.e.*, a structural transition from orthorhombic to monoclinic. At 92 K, the characterization of numerous crystallites shows that neither satellites nor diffuse streaks are observed in the [010] ED patterns; this attests of the absence of CO at this temperature. Moreover, a splitting of the Bragg reflections is systematically observed, characteristic of a monoclinic cell "$a_p\sqrt{2} \times 2a_p \times a_p\sqrt{2}$, $\beta \sim 90.8°$" (Fig. 4b), and the [010] bright field images (Fig. 4a) show the formation of a second type of twinning with respect to that observed at room temperature. The two dark field images (Fig. 4c) recorded by selecting, alternately, one split reflection out of two are perfectly complementary. This shows that, in all the crystals, there are only two variants which result from the structural transition and confirms the absence of any other phase in addition to the monoclinic one at 92 K.

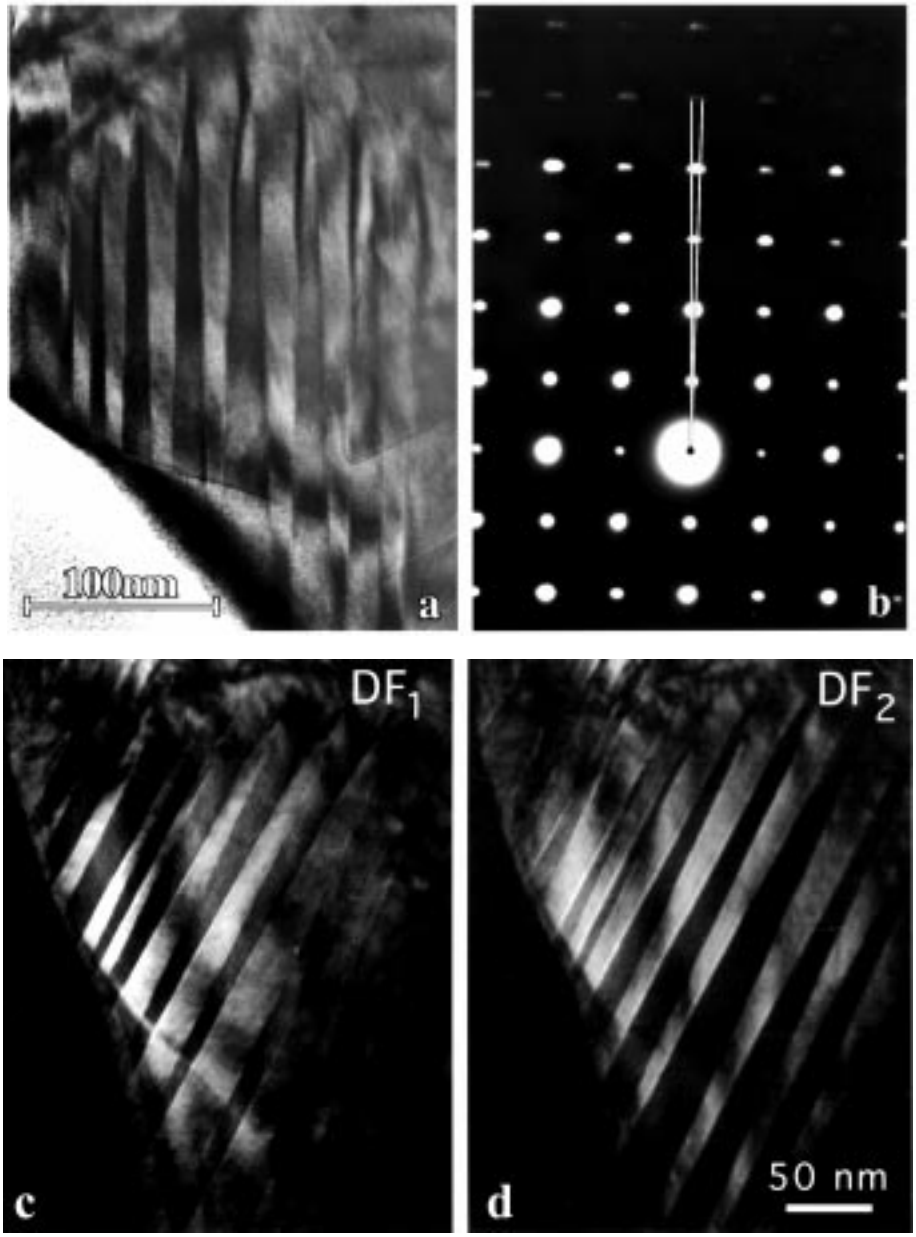

Fig. 4. $Ca_{0.92}Th_{0.08}MnO_3$ at 92 K: (a) [010] bright field images (b) [010] ED pattern showing the formation of a twinning mechanism. (c) Complementarity of the two dark field images (labelled DF1 and DF2).

The monoclinic distortion, and concomitantly the twinning, disappear abruptly at 124 K, coinciding with the temperature $T_{\rm peak}$ of the maximum of the $M(T)$ curve. The phenomenon is reversible.

Thus in the $Th_{0.08}$ phase, as well as in the $Sm_{0.15}$ one, the decrease of the magnetization and the insulating state below $T_{\rm peak}$ are connected to a structural, orthorhombic to monoclinic transition. It appears at $x = 0.08$ for the Th series, *i.e.* a value half of that found for the Sm doped phases ($x = 0.15$). This is clearly due to the different valencies of Th(+4) and lanthanides (+3).

Starting from $CaMnO_3$, this shows that, by increasing the Th^{4+} or Ln^{3+} doping connected structural-magnetic-transport transitions are induced for the same critical electron concentration $[Mn^{3+}] = 2x_{\rm Th} = x_{\rm Ln}$. For the lowest experimental temperature, 92 K, no superlattice peaks on ED patterns associated to Mn^{3+}/Mn^{4+} CO are observed. It is thus difficult to ascribe the CMR effect, for this critical electron concentration, to the CO melting by magnetic field application. It may thus be attributed to a field induced structural transition from the monoclinic insulating phase towards the orthorhombic semimetallic like one. Recent magnetostriction measurements performed on $Ca_{0.85}Sm_{0.15}MnO_3$ show that a huge field induced volume change occurs in this CMR compound [28]. However, one cannot exclude a field induced magnetic polarons destruction formed in the antiferromagnetic background.

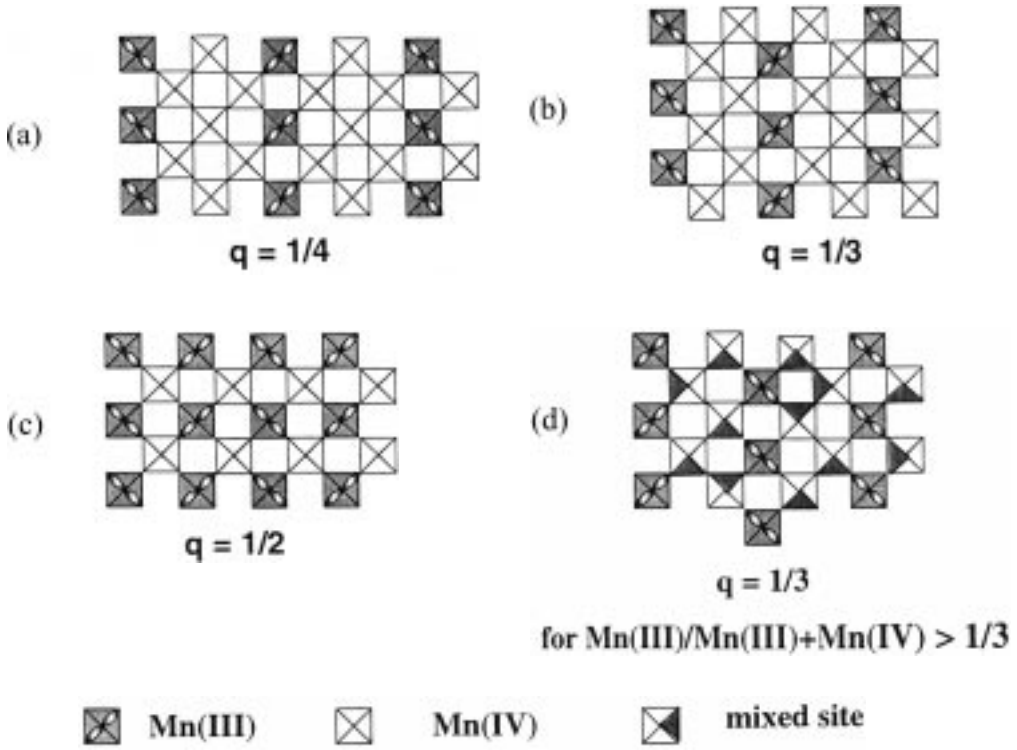

Fig. 5. Idealized models of the commensurate superstructures with (a) $a = 4\ a_{\rm p}\sqrt{2}$, (b) $a = 3\ a_{\rm p}\sqrt{2}$ and (c) $a = 2\ a_{\rm p}\sqrt{2}$. These superstructures, observed below $T_{\rm CO}$, correspond to the alternation along **a** of one Mn^{3+} stripe with three Mn^{4+} stripes, two Mn^{4+} stripes and one Mn^{4+} stripe respectively. (d) model of the superstructure obtained for $x = 0.4$, with $q = 1/3$, implying that the excess of Mn^{3+} occupy the sites of the Mn^{4+} stripes.

3.3 Short and long range charge ordering in $Ca_{1-x}Th_xMnO_3$, $0.12 < x \leq 0.30$

For $x > 0.08$, the intensity of the peak on the $M(T)$ curves decreases rapidly, whereas $T_{\rm peak}$ increases with x (see for instance $x = 0.15$, 0.20 and 0.25 in Fig. 3a). These bumps on the $M(T)$ curves are associated with a semimetallic to insulating state transition as T decreases from room temperature (Fig. 3b). This phenomenon, already observed in half-doped and electron doped manganites $Ca_{1-x}Ln_xMnO_3$, is interpreted as the result of charge ordering (CO) phenomena, due to the formation and ordering of Mn^{3+} and Mn^{4+} stripes below the transition temperature $T_{\rm CO}$ [8,12,20,26,27]. Below $T_{\rm CO}$, this results in a commensurate or incommensurate supercell characterized by the parameters $a = 1/qa_{\rm p}\sqrt{2}$, $b = 2\ a_{\rm p}$ and $c = a_{\rm p}\sqrt{2}$, where q is the amplitude of the modulation vector. In the case of $Ca_{1-x}Ln_xMnO_3$, the q value is found to be strictly equal to x, *i.e.* the Mn^{3+} concentration so that commensurate superstructures are observed for $x = 1/4$ ($a = 4a_{\rm p}\sqrt{2}$), $x = 1/3$ ($a = 3a_{\rm p}\sqrt{2}$), and $x = 1/2$ ($a = 2a_{\rm p}\sqrt{2}$) below $T_{\rm CO}$. These superstructures may correspond to the alternation along **a** of one Mn^{3+} stripe with three Mn^{4+} stripes (Fig. 5a), two Mn^{4+} stripes (Fig. 5b) and one Mn^{4+} stripe (Fig. 5c), respectively. For intermediate x values, an incommensurate distribution of these stripes is obtained.

Taking into consideration this CO model of the Mn^{3+} and Mn^{4+} stripes, and bearing in mind the tetravalency of thorium, similar modulated supercells should be expected at low temperature, below $T_{\rm CO}$, for $Ca_{1-x}Th_xMnO_3$, but with a different incommensurability vector, $q = 2x$.

The ED patterns of the different samples corresponding to $0.12 \leq x \leq 0.25$, registered at 92 K attest of the presence of extra reflections with respect to the room temperature Pnma structure. The q values, measured for about twenty crystallites per sample, are quite homogeneous. The [010] ED patterns of the $x = 0.125$ (Fig. 6a) and $x = 0.167$ samples (Fig. 6b) exhibit a quadrupling ($q = 0.25$) and a tripling ($q = 0.333$) of the "a" parameter as expected from the stripe charge ordering (see Figs. 5a and 5b respectively). Surprisingly, for $x = 0.25$, the structure is clearly incommensurate with an incommensurability vector, $q = 0.41$ (Fig. 6c) much lower than the expected value ($q = 0.50$). A plot of the q value *vs.* x (Fig. 7) allows a better comparison with the Sm-doped phases, which exhibit an ideal behavior for $x \leq 0.5$. Except the $x = 1/8$ and $x = 1/6$ samples, for which the ideal q values are obtained ($q = 1/4$ and $q = 1/3$ respectively), all the other Th samples exhibit a q value much lower than the expected one, considering the Mn^{3+} content ($q = 2x$). Moreover commensurate structures appear for irrational "$2x$" values: this is the case for $x = 0.13$ for which $q = 1/4$, but,

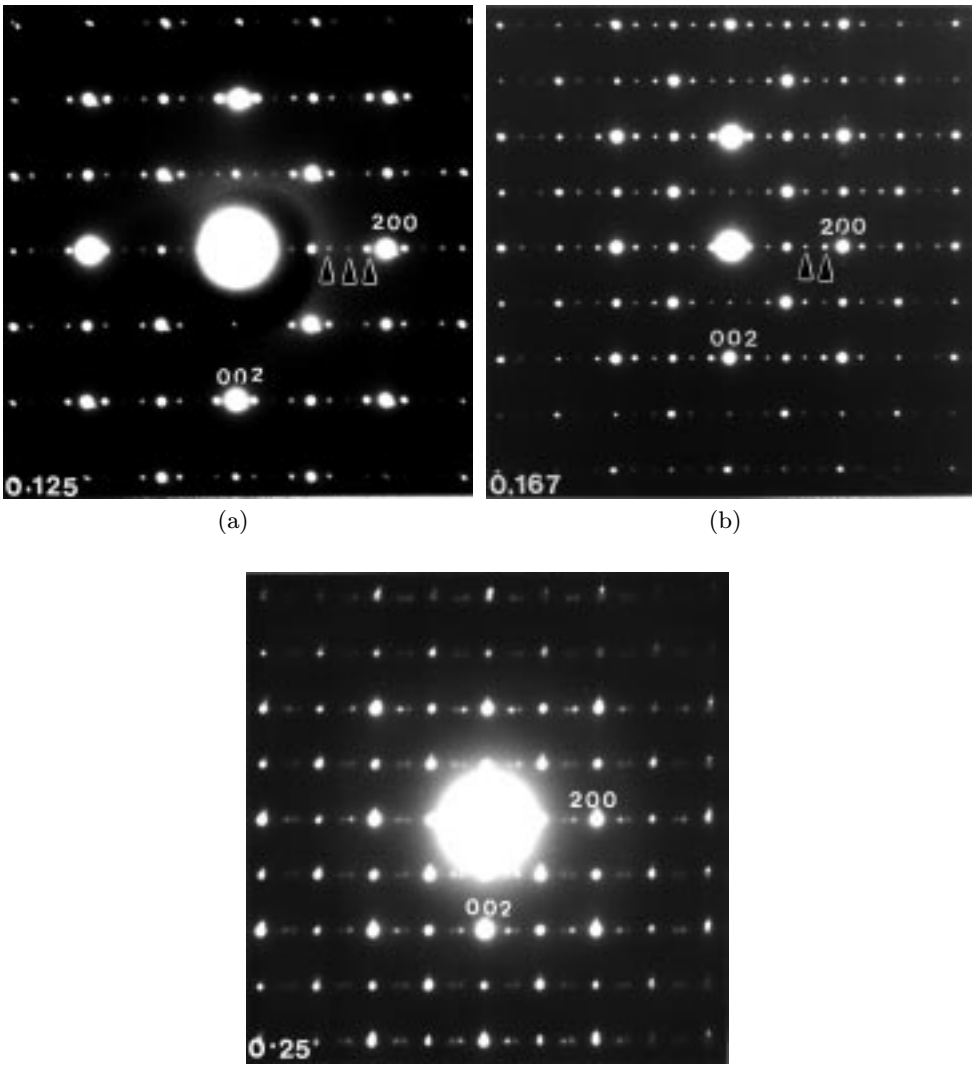

Fig. 6. [010] ED patterns of: (a) the $x = 0.125$ with $q = 0.25$ (b) $x = 0.167$ with $q = 0.333$ samples. They exhibit a quadrupling and a tripling of the "a" parameter (c) for $x = 0.25$, the structure is incommensurate ($q = 0.41$).

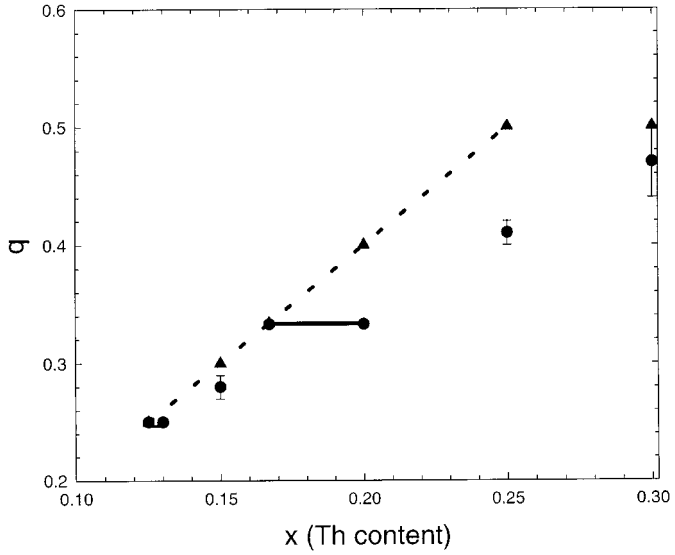

Fig. 7. Evolution of the q vector *versus* x in $Ca_{1-x}Th_xMnO_3$ (circles) and in $Ca_{1-2x}Sm_{2x}MnO_3$ (triangles) from reference [12]. The dotted oblique line corresponds to the ideal $q = 2x$ behavior and the horizontal solid line indicates the experimental domain where $q = 1/3$ in the Th series. The vertical bars on the circles indicate the q dispersion.

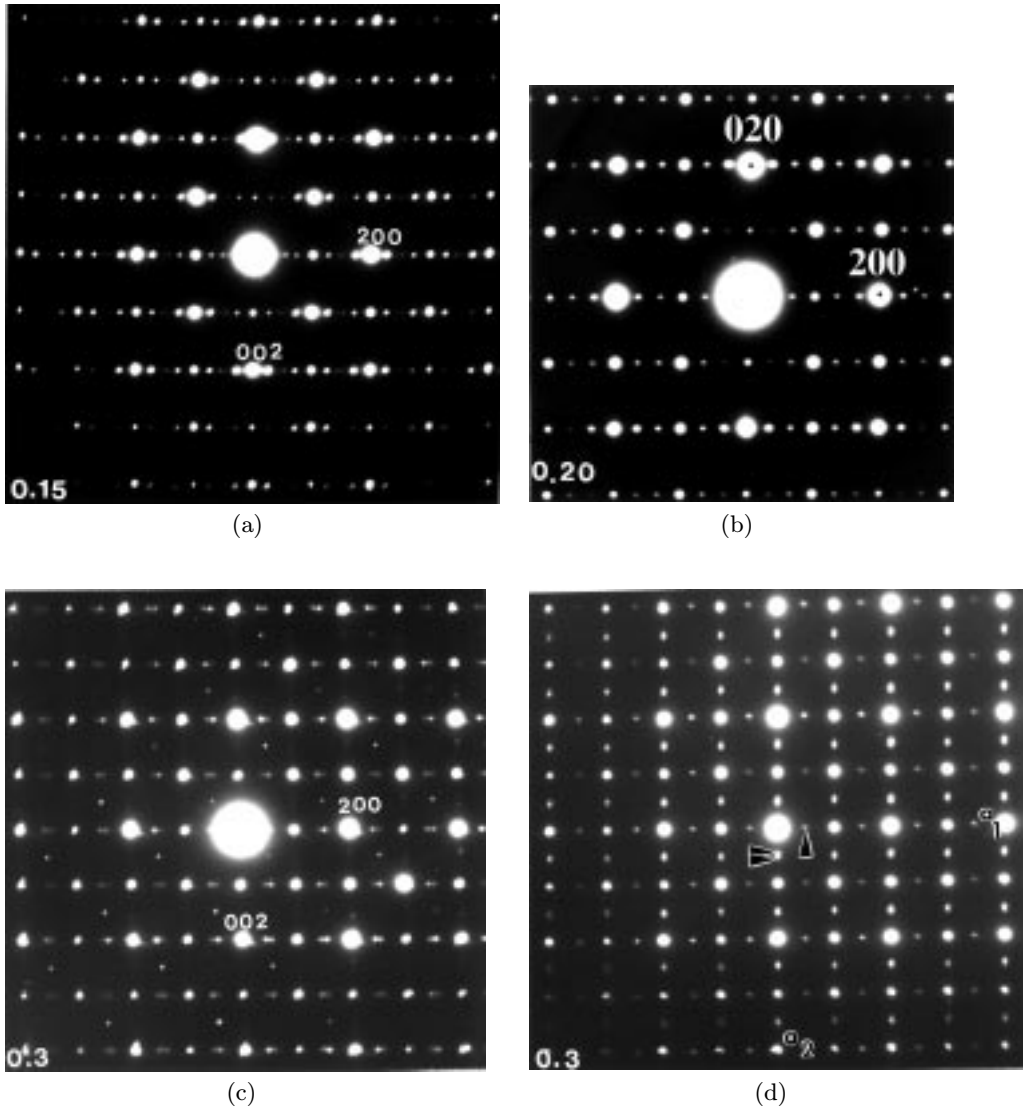

Fig. 8. [010] ED patterns of (a) $x = 0.15$ sample with $q = 0.28$ instead of 0.30 (b) $x = 0.20$, with $q = 1/3$ instead of $q = 0.40$, similar to that of the $x = 1/6$ sample. For $x = 0.3$, the q values range between 0.44 (c) and 0.5 (d).

more spectacular, for the domain $0.16 \leq x \leq 0.20$, for which $q = 1/3$, whatever x.

The images registered at 92 K allow these phenomena to be explained. This is the case for instance, of the $x = 0.15$ sample whose ED pattern (Fig. 8a) indicates a q value of 0.28 instead of 0.30. In fact, the corresponding bright field image (Fig. 9a) shows a system of large fringes, parallel to (001), with an average periodicity close to $4a_{\rm p}\sqrt{2} \approx 22$ Å, corresponding to the ideal value $q = 0.25$. Actually, several disordering phenomena are breaking this regularity, leading to $q = 0.28$. One indeed observes the modulation of the fringe contrast which locally modifies the inter-fringe distances ($3a_{\rm p}\sqrt{2}$). Moreover, these fringes are frequently shifted along **a**, forming domains a few nanometers long, and often suffer dislocation-like mechanisms. This behaviour is clearly visible by viewing the image under grazing incidence. This disordering appears with respect to $q = 0.25$, due to the disappearance of Mn^{4+} stripes. In contrast, for $x = 0.20$, the ED patterns (Fig. 8b) show a commensurate structure $q = 1/3$, instead of $q = 0.40$, similar to that of the $x = 1/6$ sample (Fig. 6b) whereas an incommensurate phase with $q = 0.40$ is expected according to the formula $Ca_{0.8}Th_{0.2}Mn^{4+}_{0.6}Mn^{3+}_{0.4}O_3$. The corresponding bright field image (Fig. 9b), which exhibits twinning domains (see ED pattern insert), confirms that the periodicity along **a**, is close to $3a_{\rm p}\sqrt{2} \approx 16.5$ Å in agreement with $q = 1/3$. This particular value of q is observed in the two variants, with a quite perfect alternation of fringes along **a**, involving a tripling of the a parameter like in the $x = 1/6$ sample. This suggests that the distribution of the charges, *i.e.* of the Mn^{3+} and Mn^{4+} species in $x = 0.20$ (Fig. 5d) differs from the one of $x = 1/6$ (Fig. 5b) by randomly introducing additional Mn^{3+} species in the Mn^{4+}

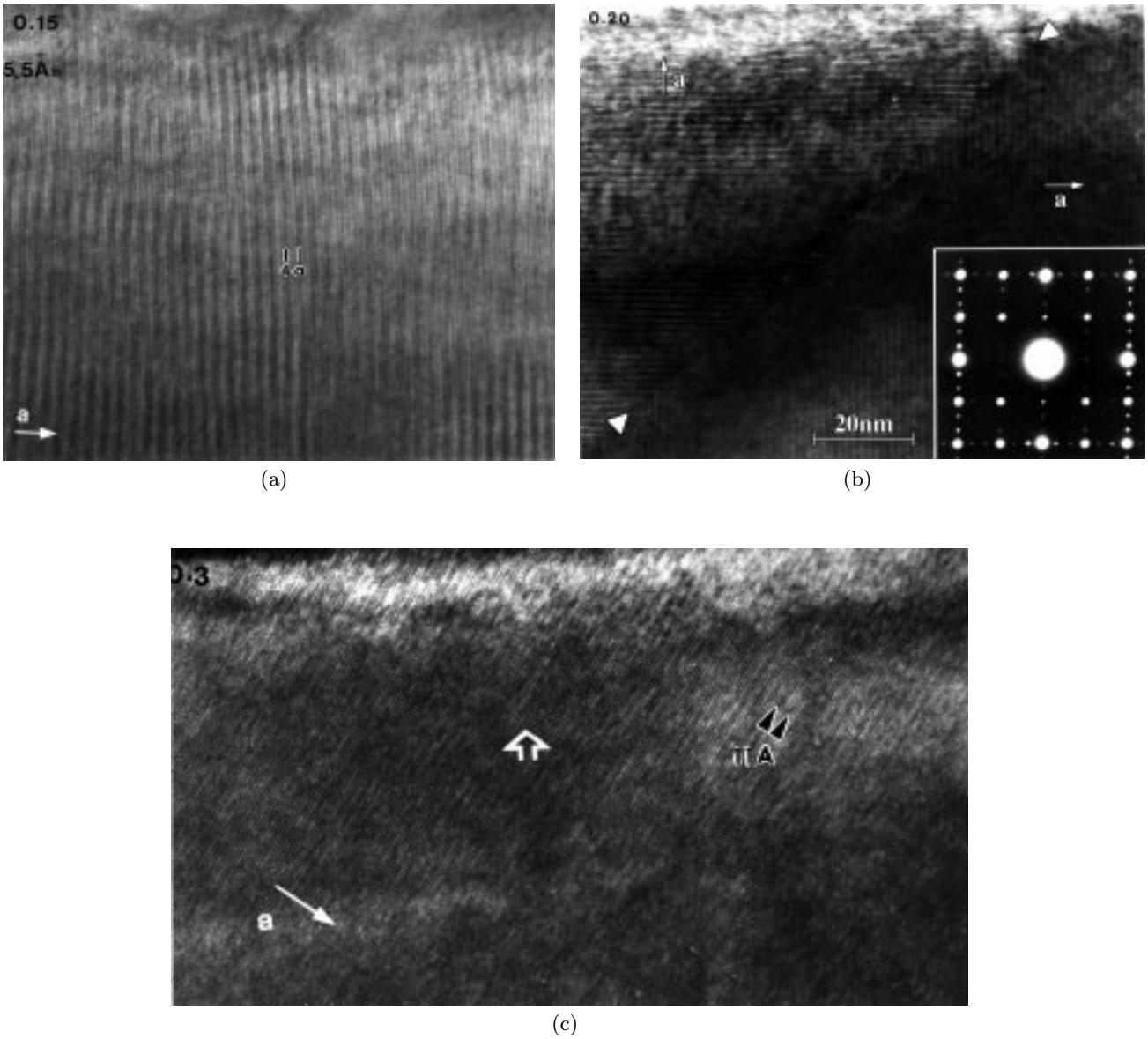

(a) (b)

(c)

Fig. 9. [010] lattice image of (a) $x = 0.15$ which exhibit a system of large fringes, parallel to (001), with an average periodicity close to $4a_p\sqrt{2} \approx 22$ Å. (b) $x = 0.20$. Example of a crystallite exhibiting twinning domains (see ED pattern in insert). The periodicity along **a**, in the two variants, is close to $3a_p\sqrt{2} \approx 16.5$ Å ($q = 1/3$). (c) $x = 0.3$ and $q = 0.5$: the fringes are 11 Å spaced, but in some areas, the modulation is no more visible (white arrow).

stripes. In other words, the $x = 0.20$ sample may consist of a stacking along **a** of single Mn^{3+} stripes with double mixed valent Mn^{3+}/Mn^{4+} stripes (Fig. 5d). This effect for $Ca_{1-x}Th_xMnO_3$ contrasts with that reported for $Ca_{1-x}Sm_xMnO_3$ ($0.20 < x \leq 0.5$) for which no mixed Mn^{3+}/Mn^{4+} stripes were observed [12]. However, the lattice images do not allow to distinguish the different types of distorted octahedra within one stripe. High resolution image will be required to get information about this issue.

The tendency to lower the q value with regard to the $2x$ value increases with x. For $x = 0.25$, the average q value is 0.41 instead of 0.50 and for $x = 0.30$, q values ranging from 0.44 to 0.50 instead of 0.60 are observed, as illustrated in Figures 8c–8d. In Figure 8c ($x = 0.30$), the q value is close to 0.44, as observed from the clear separation of the additional 0001 and $100\overline{1}$ satellites (using four hklm Miller indices). Figure 8d provides another example of one $x = 0.30$ crystallite with twin modulated domains: along the vertical direction (noted a_2^*), the elongated spots result from a q value which is very close but slightly inferior to 0.5, whereas, along the horizontal direction (noted a_1^*), sharp single reflections show that $q = 0.5$, *i.e.* the 0001 satellite is exactly superposed on the $100\overline{1}$ one. The corresponding lattice image (Fig. 9c) shows that one bright fringe alternates with one grey fringe, so that the periodicity is close to $2a_p\sqrt{2} = 11$ Å, in agreement with

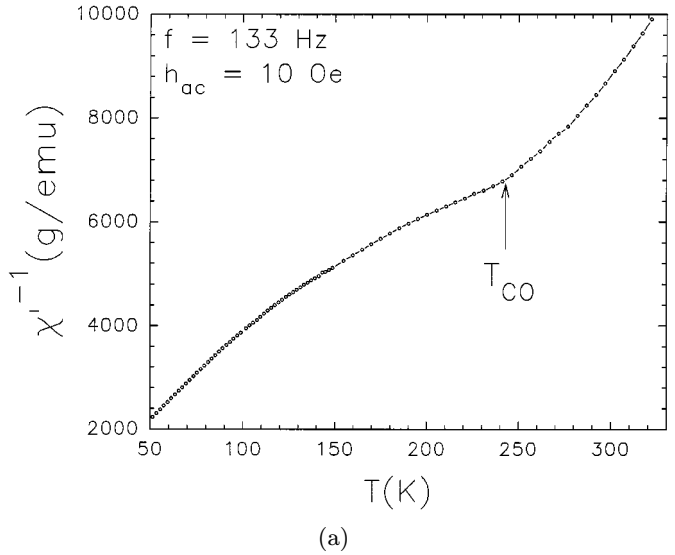

(a)

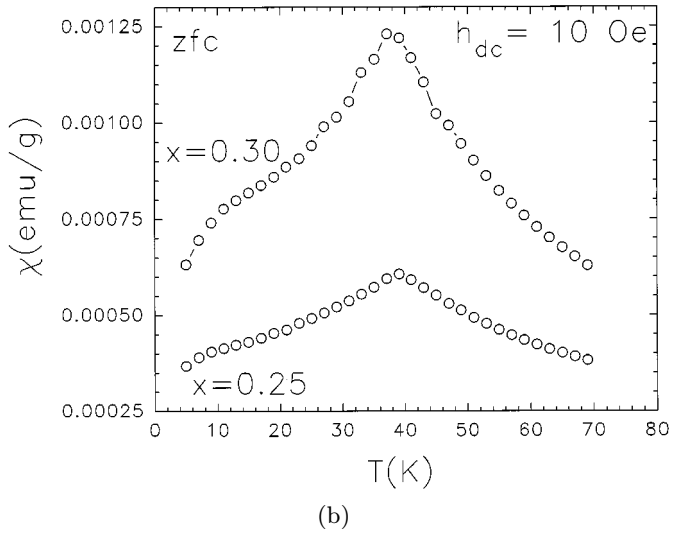

(b)

Fig. 10. $\chi'^{-1}(T)$ curve for (a) $x = 0.25$ (b) $\chi(T)$ curves for $x = 0.25$ and 0.30, from magnetization measurements.

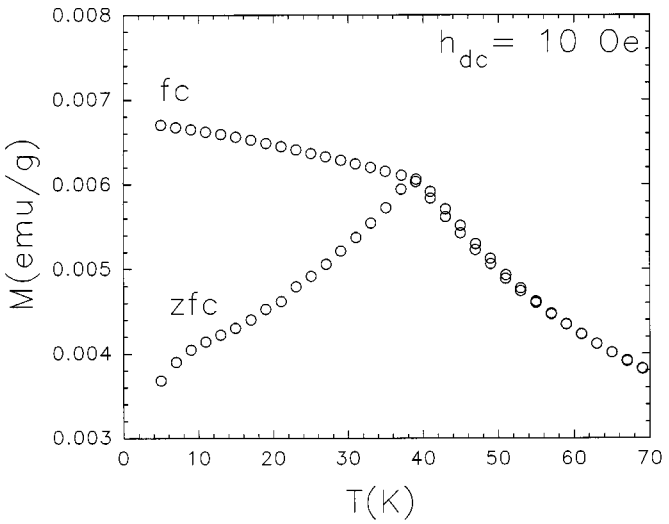

(a)

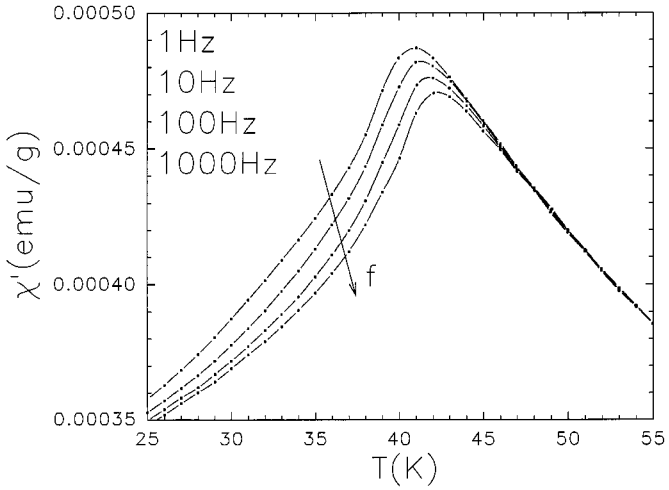

(b)

Fig. 11. FC-ZFC magnetization curves (a) and frequency dependence of the cusp temperature (b) for $Ca_{0.75}Th_{0.25}MnO_3$.

the model of Figure 5c. This suggests that for $x = 0.30$, one Mn^{3+} stripe alternates with one mixed valent stripe (0.2 Mn^{3+}/0.8 Mn^{4+}) along **a**. However, the variation of the fringes (one bright-one grey) is sometimes barely detectable with only 5.5 Å as visible periodicity (see white arrow). The observation of fringe systems in the [010] lattice images implies that the ordering is established along the viewing direction, namely **b**.

The disappearance of these fringe systems can therefore be correlated either to a partial (only along **b**) or total (3D) loss of the perfect ordering. The first case (only along **b**) involves short range ordering phenomena whereas the second case involves the coexistence of small ordered and disordered areas.

This deviation of the q value, characteristic of the charge ordering, ($q < 2x$) must be correlated with the magnetic measurements. The latter show indeed that the bump of the $M(T)$ curves tends to disappear for higher x values and is hardly detectable for $x = 0.30$. Nevertheless the $\chi'^{-1}(T)$ curve (Fig. 10a) shows a slight slope variation at 250 K, for $x = 0.25$, in agreement with the T_{CO} deduced from electron microscopy observations. The $\chi(T)$ curve shows a clear cusp at $\approx$ 40 K for $x = 0.25$ and $x = 0.30$ (Fig. 10b), suggestive of a spin glass like behavior. For $x = 0.25$, the quasi T independent field cooled branch observed on the FC-ZFC magnetization curves (Fig. 11a) and the frequency dependence of the cusp temperature (Fig. 11b) expected for a spin-glass [29] confirm this hypothesis. It is most probable therefore that the destabilisation of charge ordering as shown from electron microscopy which is induced by high Th^{4+} contents ($x \approx 0.25$–0.30) tends to weaken the CO state at low temperature. As a consequence the AFM structure is strongly

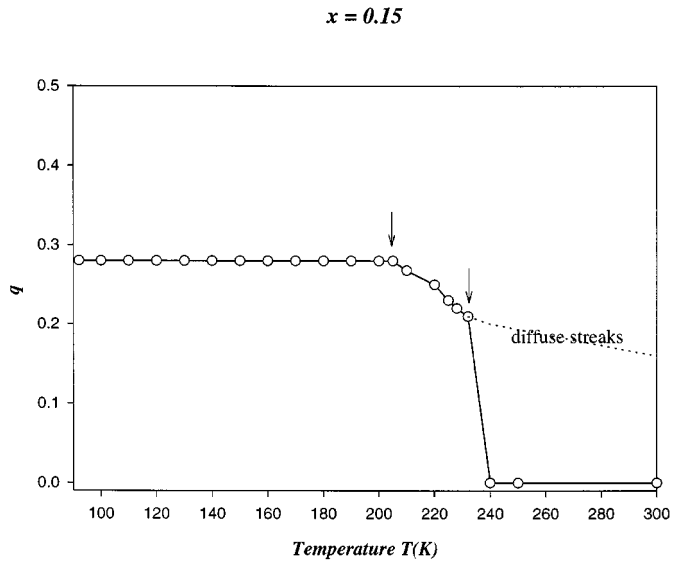

(a)

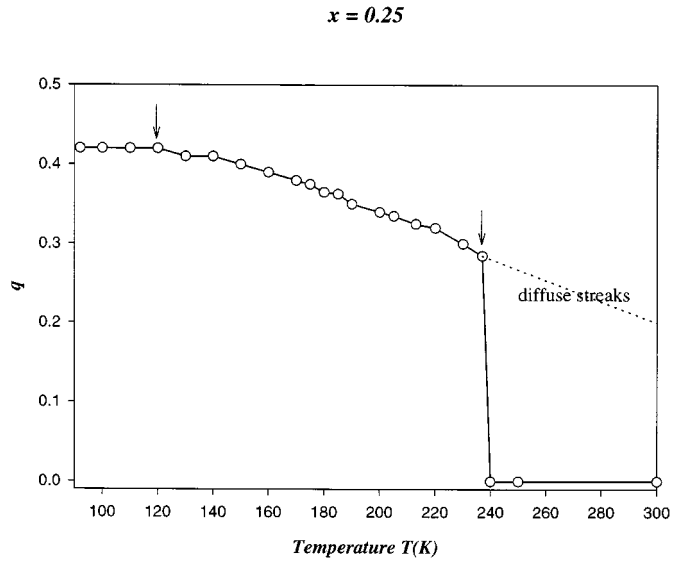

(b)

Fig. 12. Evolution of q *vs.* T. (a) $x = 0.15$ and (b) $x = 0.25$. Between 235 K and 300 K, the presence of very weak and diffuse streaks, but without any measurable nodes, is illustrated by the dotted lines.

disturbed by so restoring FM interactions. Consequently a spin glass like behavior is favoured. This assumption is in agreement with the lack of spin glass behavior for the $Ca_{1-x}Sm_xMnO_3$ series.

3.4 Nature of the charge order-disorder transition (x = 0.15 and 0.25)

The q values were recorded as a function of temperature, slowly warming the sample from 92 K to roomtemperature by steps of 5 K. Two examples of the evolution of

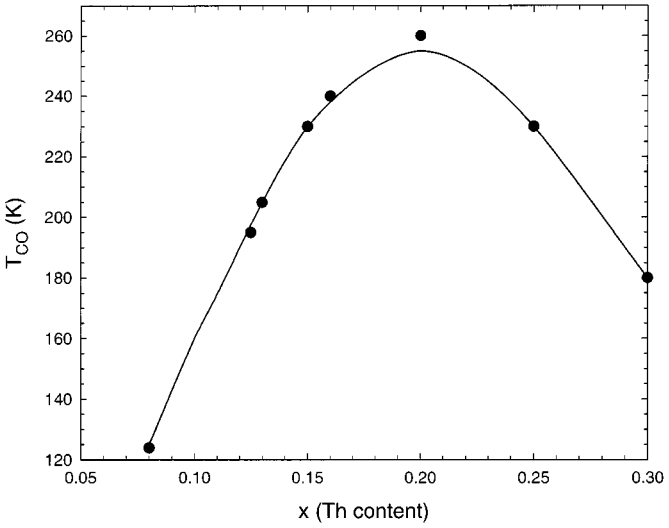

Fig. 13. Evolution of T_{CO} *vs.* x in $Ca_{1-x}Th_xMnO_3$. Black circles are T_{CO} obtained from ED observations, except for $x = 0.08$ where it corresponds to the orthorhombic-monoclinic transition. The solid line is drawn from T_{peak} on the $M(T)$ curves.

q *vs.* T are given for $x = 0.15$ and $x = 0.25$, in Figures 12a and 12b. At lower temperature (92 K) all the $q(T)$ curves exhibit a plateau characteristic of the charge ordered structure, *i.e.* $q = 0.28$ for $x = 0.15$ (Fig. 12a) and $q = 0.41$ for $x = 0.25$ (Fig. 12b). Then beyond a certain temperature, T_{plat} (see arrows on the $q(T)$ curves), q decreases as T increases, in a more or less abrupt way, and simultaneously the intensity of the satellites decreases, as for the $Ca_{1-x}Sm_xMnO_3$ manganites. However the Th-doped manganites differ from the Sm-doped ones by the width of the transition. For the Sm-doped oxides, the decrease of the intensity of the satellites is rapid, so that it is easy to determine T_{CO}. In the Th-doped phases, the intensity of the satellites decreases very slowly, and one observes diffuse streaks near the transition over a large temperature range, so that T_{CO} is more difficult to determine (this is illustrated by dotted lines between 235 K and 300 K). Consequently the width of the transition, $\Delta T = T_{CO} - T_{plat}$, is much broader for Th phases than for Sm phases, and moreover increases dramatically with x (compare for example $\Delta T = 25$ K for $x = 0.15$ to $\Delta T = 115$ K for $x = 0.25$).

The T_{CO} temperatures deduced from ED observations are in good agreement with the values deduced from the M(T) curves, as shown in the $T_{CO}(x)$ curve of Figure 13. This curve is very similar to the one previously observed for the samarium series, showing that it is mainly the electron concentration, *i.e.* $[Mn^{3+}] = x_{Sm} = 2x_{Th}$, which determines T_{CO}. This effect largely overcomes the effects of average A-site cationic size and A-site cationic sizemismatch as the nature of the lanthanide is changed in both series [19]. Note that in both series T_{CO} reaches a maximum for a Mn^{3+} concentration close to 0.40.

4 Concluding remarks

The comparison of the electron doped manganites $Ca_{1-x}Th_xMnO_3$ and $Ca_{1-x}Sm_xMnO_3$ shows that the magnetic and transport transitions observed in these systems are closely connected to structural transitions and that the electron carrier density (Mn^{3+} concentration) plays a major role in such effects. For low electron concentration, both Th ($x \sim 0.08$) and Sm ($x \sim 0.15$) doped phases exhibit a similar orthorhombic-monoclinic transition which accompanies the FM/AFM competition. For higher electron concentrations the Th doped phases still exhibit charge ordering phenomena like the Sm doped phases, but the ordering becomes less perfect ($q < 2x$). The tendency towards a weakening of this charge ordering increases as the thorium content increases, leading finally, for the highest contents ($x = 0.25$ and 0.30) to a spin glass like behaviour. This demonstrates the existence of a competition between ferromagnetic and antiferromagnetic interactions. Such a difference with respect to samarium compounds is also observed by comparing the Th-doped manganites with other Ln^{3+} doped manganites which have an average $Ca_{1-x}Ln_x$ cationic radius close to $Ca_{1-x/2}Th_{x/2}$ [19]. This suggests that the different CO phenomena observed for thorium, compared to lanthanides, are not due to size effect but result from a different local effect of the Th^{4+}/Ca^{2+} substitution on the structure, compared to Ln^{3+} and Ca^{2+}. The larger charge difference between Th^{4+} and Ca^{2+} species (charge mismatch), may then induce local distortions and consequently influence the ordering of the Mn^{3+} and Mn^{4+} species. In this respect, the existence of spin glass like properties for $Ca_{0.75}Th_{0.25}Mn^{3.5^+}O_3$ in contrast to $Ca_{0.5}Sm_{0.5}Mn^{3.5+}O_3$ may result from the A-site charge mismatch between Ca^{2+} and Th^{4+} that disturbs the Mn^{3+}/Mn^{4+} charge ordering process.

The authors gratefully acknowledge the University of Caen, for supporting this work through a position of Associate Professor.

References

1. R.M. Kusters, J. Singleton, D.A. Keen, R. McGreevy, W. Hayes, Physica B **155**, 362 (1989).
2. K. Chahara, T. Ohno, M. Kasai, Y. Kozono, Appl. Phys. Lett. **63**, 1990 (1993).
3. S. Jin, T.H. Tiefel, M. McCormack, R.A. Fasnacht, R. Ramesh, L.H. Chen, Science **264**, 413 (1994).
4. H.L. Ju, C. Kwon, Q. Li, R.L. Green, T. Venkatesen, Appl. Phys. Lett. **65**, 2108 (1994).
5. R. Von Helmolt, J. Wecker, K. Samwer, K. Barner, J. Magn. Magn. Mater. **151**, 411 (1995).
6. C. Zener, Phys. Rev. **82**, 403 (1951).
7. H.Y. Hwang, T.T. Palstra, S.W. Cheong, B. Battlog, Phys. Rev. B **52**, 15046 (1995).
8. Z. Jirak, S. Krupicka, Z. Simsa, M. Dlouha, S. Vratislav, J. Magn. Magn. Mater. **53**, 153 (1985).
9. J.B. Goodenough, Phys. Rev. **100**, 564 (1955).
10. E.O. Wollan, W.C. Koehler, Phys. Rev. **100**, 545 (1955).
11. C.H. Chen, S.W. Cheong, Phys. Rev. Lett. **76**, 4042 (1996).
12. M. Hervieu, A. Barnabé, C. Martin, A. Maignan, F. Damay, B. Raveau, Eur. Phys. J. B **8**, 31 (1999).
13. C. Martin, A. Maignan, F. Damay, M. Hervieu, B. Raveau, J. Solid State Chem. **134**, 198 (1997).
14. V.A. Bokov, N.A. Grigoryan, M.F. Bryzhina, Phys. Stat. Sol. **20**, 745 (1967).
15. W. Bao, J.D. Axe, C.H. Chen, S.W. Cheong, Phys. Rev. Lett. **78**, 543 (1997).
16. T. Murakami, D. Shindo, H. Chiba, M. Kikuchi, Y. Syono, Phys. Rev. B **55**, 1 (1997).
17. H. Chiba, M. Kikuchi, K. Kusaba, Y. Muraoka, Y. Syono, Solid St. Commun. **99**, 949 (1996).
18. I.O. Troyanchuk, N.V. Samsonenko, H.Szymczak, A. Nabialek, J. Solid State Chem. 131, 144 (1997).
19. A. Maignan, C. Martin, F. Damay, B. Raveau, Chem. Mater. **10**, 950 (1998).
20. A. Barnabé, M. Hervieu, C. Martin, A. Maignan, B. Raveau, J. Appl. Phys. **84**, 10 (1998).
21. M. Hervieu, G. Van Tendeloo, V. Caignaert, A. Maignan, B. Raveau, Phys. Rev. B. **53**, 21 (1996).
22. W. Schuddinck, O. Richard, G. Van Tendeloo, F. Millange, M. Hervieu, B. Raveau, Acta Cryst. (in press).
23. G. Van Tendeloo, O. Richard, W. Schuddinck, M. Hervieu, Electron Microscopy **1**, 383 (1998).
24. A. Maignan, C. Martin, F. Damay, B. Raveau, J. Hejtmanek, Phys. Rev. B **58**, 2758 (1998).
25. J. Van den Brink, D. Khomskii, Phys. Rev. Lett. **82**, 1016 (1999).
26. P.G. Radaelli, D.E. Cox, M. Marezio, C.H. Chen, S.W. Cheong, Phys. Rev. B **55**, 3015 (1997).
27. J. Blasco, J. Garcia, J.M. de Teresa, M.R. Ibarra, J. Perez, P.A. Algarabel, C. Marquina, C. Ritter, J. Phys.-Cond. Matter **9**, 10321 (1997).
28. R. Mahendiran, M.R. Ibarra, C. Martin, A. Maignan, B. Raveau (to be published).
29. J.A. Mydosh, *Spin glasses* (Taylor & Francis Ltd, London, 1993).